

SEARCH FOR CARBON MONOXIDE IN THE ATMOSPHERE OF THE TRANSITING EXOPLANET HD 189733b

JEAN-MICHEL DÉSSERT¹, ALAIN LCAVELIER DES ETANGS¹, GUILLAUME HÉBRARD¹, DAVID K. SING¹, DAVID EHRENREICH²,
ROGER FERLET¹, AND ALFRED VIDAL-MADJAR¹

Draft version July 23, 2018

ABSTRACT

Water, methane and carbon-monoxide are expected to be among the most abundant molecules besides molecular hydrogen in the hot atmosphere of close-in extrasolar giant planets. Atmospheric models for these planets predict that the strongest spectrophotometric features of those molecules are located at wavelengths ranging from 1 to 10 μm making this region of particular interest. Consequently, transit observations in the mid-IR allow the atmospheric content of transiting planets to be determined. We present new primary transit observations of the hot-jupiter HD 189733b, obtained simultaneously at 4.5 and 8 μm with the Infrared Array Camera (IRAC) onboard the *Spitzer Space Telescope*. Together with a new refined analysis of previous observations at 3.6 and 5.8 μm using the same instrument, we are able to derive the system parameters, including planet-to-star radius ratio, impact parameter, scale of the system, and central time of the transit from fits of the transit light curves at these four wavelengths. We measure the four planet-to-star radius ratios, to be $(R_p/R_\star)_{3.6\ \mu\text{m}} = 0.1545 \pm 0.0003$, $(R_p/R_\star)_{4.5\ \mu\text{m}} = 0.1557 \pm 0.0003$, $(R_p/R_\star)_{5.8\ \mu\text{m}} = 0.1547 \pm 0.0005$, and $(R_p/R_\star)_{8\ \mu\text{m}} = 0.1544 \pm 0.0004$. The high accuracy of the planet radii measurement allows the search for atmospheric molecular absorbers. Contrary to a previous analysis of the same dataset, our study is robust against systematics and reveals that water vapor absorption at 5.8 μm is not detected in this photometric dataset. Furthermore, in the band centered around 4.5 μm we find a hint of excess absorption with an apparent planetary radius $\Delta R_p/R_\star = 0.00128 \pm 0.00056$ larger (2.3σ) than the one measured simultaneously at 8 μm . This value is 4σ above what would be expected for an atmosphere where water vapor is the only absorbing species in the near infrared. This shows that an additional species absorbing around 4.5 μm could be present in the atmosphere. Carbon monoxide (CO) being a strong absorber at this wavelength is a possible candidate and this may suggest a large CO/H₂O ratio between 5 and 60.

Subject headings: eclipses planetary systems stars: individual: (HD189733b) techniques: photometric

1. INTRODUCTION

The theory of transmission spectroscopy was developed in detail by the pioneering works of Seager & Sasselov (2000), Brown (2001), Burrows et al. (2001), and Hubbard et al. (2001). This method is now widely used to probe the atmospheric structure and composition of the transiting planets. Applied to the first transiting extrasolar planet known, HD 209458b, this method allowed for the first detection of an extrasolar planetary atmosphere (Charbonneau et al. 2002), and of the discoveries of an escaping exosphere (Vidal-Madjar et al. 2003, 2004, 2008; Ehrenreich et al. 2008), and a hot hydrogen layer in the middle atmosphere (Ballester et al. 2007).

HD 189733b is a transiting hot-jupiter which orbits a small and bright main sequence K star, and shows a transit occultation depth of $\sim 2.5\%$ (Bouchy et al. 2005). The planet has a mass of $M_p = 1.13$ Jupiter mass (M_J) and a radius of $R_p = 1.16$ Jupiter radius in the visible (Bakos et al. 2006b; Winn et al. 2007). The short period of the planet (~ 2.21858 days) is known with high accuracy (Hébrard & Lecavelier des Etangs 2006; Knutson et al. 2009). Sodium in the atmosphere of the planet has been detected through ground-based observations (Red-

field et al. 2008). Using the Advanced Camera for Survey aboard the *Hubble Space Telescope* (HST), Pont et al. (2008) detected atmospheric haze interpreted as Mie scattering by small particles (Lecavelier des Etangs et al. 2008a).

The red part of the visible to the Infrared (IR) is a spectral region of particular interest to detect molecular species using transmission spectroscopy (e.g., Tinetti et al. 2007). The rotational-vibrational transition bands of water (H₂O), carbon monoxide (CO), and methane (CH₄) are anticipated to be the primary sources of non-continuum opacity in hot-Jovian planets. Their relative abundances are determined by the C/O ratio (Liang et al. 2003, 2004; Kuchner & Seager 2006). Carbon monoxide is expected to be the dominant carbon-bearing molecule at high temperatures and CH₄ the dominant one below ~ 1000 K (Kuchner & Seager 2006; Cooper & Showman 2006; Sharp & Burrows 2007). In the case of HD 209458b's atmosphere, Brown et al. (2002) and Deming et al. (2005) reported exploratory attempts to detect CO during transit from ground based observations. In the same atmosphere, the possible presence of H₂O (Barman et al. 2005), TiO and VO (Désert et al. 2008; Sing et al. 2008a,b), and the detection of the main constituent, H₂, through Rayleigh scattering (Lecavelier des Etangs 2008b), have been reported using observations in the visible from the Space Telescope Imaging Spectrograph aboard HST.

Richardson et al. (2006) obtained the first infrared (IR)

¹ Institut d'astrophysique de Paris, CNRS (UMR 7095), Université Pierre et Marie Curie, 98 bis boulevard Arago, 75014 Paris, France

² Laboratoire d'astrophysique de l'observatoire de Grenoble, Université Joseph Fourier, CNRS (UMR 5571), BP53 38041 Grenoble cedex 9, France

transit measurement for this planet using the *Spitzer Space Telescope* (Werner et al. 2004) at $24\ \mu\text{m}$, and derived the planet radius with high accuracy.

HD 189733b has been observed at $8\ \mu\text{m}$ (Channel 4) with the Infrared Array Camera (IRAC; Fazio et al. 2004) aboard *Spitzer*. The planet-to-star radius ratio at $8\ \mu\text{m}$ was found to be $(R_p/R_*)_{8\ \mu\text{m}} = 0.1545 \pm 0.0002$ (Knutson et al. 2007a). Agol et al. (2008) also observed this planet at $8\ \mu\text{m}$ during 7 primary transits and used the high photometrical precision at this wavelength for the searching companions using *Transit Timing Variations* (TTV) method.

More recently, secondary eclipse measurements revealed the presence of water, carbon monoxide and carbon dioxide in the dayside emission spectrum of the planet, between 1.5 and $2.5\ \mu\text{m}$ (Swain et al. 2009), and water absorption with the possible presence of carbon monoxide as a contributor near the *Spitzer*/IRAC $4.5\ \mu\text{m}$ (Grillmair et al. 2008).

Results at $3.6\ \mu\text{m}$ and $5.8\ \mu\text{m}$ (Channel 1 and 3) from primary transit observations of HD 189733b using *Spitzer*/IRAC have already been published but led to two different conclusions (Ehrenreich et al. 2007; Beaulieu et al. 2008). From the analysis of Beaulieu et al. (2008); Tinetti et al. (2007) concluded that water vapour is detected in the atmosphere of the planet, whereas Ehrenreich et al. (2007) claim that uncertainties on the measurements are too large to draw any firm conclusions. Independently, a detection of water and methane has also been obtained using observations between 1.5 and $2.5\ \mu\text{m}$ from the Near Infrared Camera and Multi-Object Spectrometer aboard HST (Swain et al. 2008).

Here we describe *Spitzer* observations collected during two primary transits of HD 189733b, with the intent to measure its radius at the four IR bandpasses of the IRAC instrument. We analyze, in a consistent way, the observations from four bands centered at 3.6 , 4.5 , 5.8 and $8\ \mu\text{m}$. We probe the planet atmospheric composition by comparing results from these four photometric bands. We first describe the observations and data reduction in Sect. 2. In Sect. 3, we describe the model and techniques used to estimate the physical and orbital parameters of HD 189733b. We discuss our results in Sect. 4 in the light of previous analysis and theoretical predictions. We finally summarize our work in Sect. 5.

2. OBSERVATIONS AND DATA REDUCTION

2.1. Observations

We obtained *Spitzer* Guest Observer’s time in Cycle 3 and 4 (PI: A. Vidal-Madjar; program IDs 30590 & 40732), in the 4 *Spitzer*/IRAC bandpasses. Our primary scientific objectives were to detect the main gaseous constituents (H_2O and CO) of the atmosphere of the hot-Jupiter HD 189733b. First observations of the system were performed on 2006 October 31 simultaneously at 3.6 and $5.8\ \mu\text{m}$ (channels 1 and 3) (Ehrenreich et al. 2007). The second part of the program was completed on November 23, 2007 using the 4.5 and $8\ \mu\text{m}$ channels (channels 2 and 4) following the same methods. The system was observed using IRAC’s stellar mode during 4.5 hours for each visit, upon which 1.8h was spent in planetary transit. The observations were split in consecutive subexposures at a cadence of $0.4\ \text{s}$ for channels 1 and 2 and $2.0\ \text{s}$ for channels 3 and 4. We obtained a total of

1936 frames for channels 1 and 3, and 1920 frames for channels 2 and 4.

While planning the observation in the Astronomical Observing Request (AOR) format, we carefully selected a pixel area avoiding dead pixels. We also purposely did not dither the pointing in order to keep the source on a given pixel of the detector. Doing so minimizes errors from imperfect flat-field corrections and thus increase the photometric accuracy. This common observational strategy matches that of recent *Spitzer* observations of HD 189733 and GJ 436 (Knutson et al. 2007; Deming et al. 2007, Gillon et al. 2007; Agol et al. 2008)

2.2. Data reduction

We used the *Spitzer*/IRAC Basic Calibrated Data (BCD) frames in the following analysis. These frames are produced by the standard IRAC calibration pipeline and include corrections for dark current, flat-fielding, detector nonlinearity, and conversion to flux units. We first find the center of the PSF of the star to a precision of 0.01 pixel using the DAOPHOT-type Photometry Procedures, CNTRD, from the IDL Astronomy Library³, which computes the centroid of a star using a derivative search. We find that the position of the center of the star varied by only less than 10% of a pixel during the whole observation. We also tested the position of the centroid of the star using GCNTRD, which computes the stellar centroid by Gaussian fitting. As a final test, we used a weighted-position sum of the flux procedure in a 5×5 pixel box centered on the approximate position of the star. These two last methods give very similar results, which are in agreement within 0.02% with the positions extracted using CNTRD. We used the APER routine, which we customized to perform a weighted aperture photometry by summing the weighted background-subtracted flux, on each pixel, within an aperture of a given radius (Horne 1986; Naylor 1998). We used a radius of 5 pixels to minimize the contribution of HD 189733B (Bakos et al. 2006a), the closest star in the field of view. We checked that our results remain the same when using a radius varying from 4 to 6 pixels. The background level for each image was determined with APER by the median value of the pixels inside an annulus, centered on the star, with an inner and outer radii of 16 and 18 pixels, respectively. This constant level is subtracted from each pixel of a subexposure to create the background-subtracted image. The background errors are dominated by statistical fluctuations. The PSF, used for weighting, is estimated in each channel as the median of the background-subtracted fluxes. The estimated error on the weighted integrated flux is calculated as the square-root of the photon-noise quadratic sum (Horne 1986; Naylor 1998). The four raw weighted light curves obtained with this method are plotted in the top panel of Fig. 1. After producing a time series for each channel, we iteratively select and trim outliers greater than 3σ by comparing the measurements to a transit light curve model. Doing so, we remove any remaining points affected by transient hot pixels. We discarded 24, 26, 46 and 19 exposures in channel 1 to 4 respectively, which represent 1 to 2% of the total number of data points.

³ <http://idlastro.gsfc.nasa.gov/homepage.html>

3. FITTING THE SPITZER TRANSIT LIGHT CURVE

3.1. Out-of-Eclipse Baseline

Because of instrumental effects, the measured stellar flux out-of-transit is not constant, but is seen to vary in time. To correct for the instrumental effects, we define a baseline function of time for each Channel. The baseline function is time- and wavelength-dependent and is used to normalize a given time series. We find that a linear function of time represents well the data in channels 1 and 2. On the other hand, in Si:As based detectors (channels 3 and 4), the effective gain, and thus the measured flux in individual pixels, drift non linearly over time. This effect, called detector ramp, is well documented (Deming et al. 2005, 2006; Harrington et al. 2007; Knutson et al. 2007). To correct for the ramp and other baseline effects, we adopted a non-linear function of time $F_{baseline} = A_0 + A_1 \times t + A_2 \log(t - t_0) + A_3 \log^2(t - t_0)$, where $F_{baseline}$ is the flux of the central star HD189733 without planetary transit and t_0 was fixed to a time a few minutes before the first observations. As a check, we also tested linear, polynomial and exponential baseline functions but find that the logarithmic baseline provides the best results for channels 3 and 4 (see also Sect. 4). We find that baselines other than logarithmic introduce significant systematic errors when determining planetary parameters as seen in Fig. 2. We fit the detector correction coefficients simultaneously with the transit-related parameters, allowing us to take into account how changes in the correction coefficients may impact the transit parameters.

3.2. Pixel-phase effect correction

Telescope jitter and intra-pixel sensitivity variations are also responsible for fluctuations seen in the raw light curves (Fig. 1 upper panel), most severe in channel 1. We find that the pixel-phase effect is negligible in our dataset for the three channels 2, 3 and 4. A description of this effect is given in the *Spitzer*/IRAC data handbook (Reach et al. 2006, p. 50; Charbonneau et al. 2005). The method reported by Morales-Calderón et al. (2006) and also applied by the two previous analyses of the present dataset for channel 1 and 3 (Ehrenreich et al. 2007; Beaulieu et al. 2008) consists in calculating a pixel-phase dependent correction by fitting the light curve variations induced by this effect using a function of one single parameter for the X and Y target positions. We find that this single order function, described with only one parameter, poorly corrects the light curves for the pixel-phase effect, and thus, systematics remains in the residuals (Sect. 4 and Fig. 3). We conclude that this function (Reach et al. 2006) is not appropriate to high precision photometry. To better decorrelate our signal from pixel-phase variations, we adopted a different correction, based on a quadratic function as described by Knutson et al. (2008) where we added a cross term (K_5), $F_{corr} = F(1 + K_1(x - x_0) + K_2(x - x_0)^2 + K_3(y - y_0) + K_4(y - y_0)^2 + K_5(x - x_0)(y - y_0))$, where x_0 and y_0 are the integer pixel numbers containing the source centroid and F is the measured flux of the central star HD 189733. The K_i coefficients are the decorrelation factors that have to be derived from fits to the the transit lightcurve (TLC). A quadratic function of X and Y, with five parameters, improves the fit compared to a linear function, from a χ^2 of 2077 to 1947 for

$n = 1912$ degrees of freedom. Introduction of the cross term (K_5) also slightly improved the fit. We find that adding higher-order terms to this equation does not improve the fit for channel 1. As an additional test, we applied this decorrelation procedure to one of the bright stars in the field of view, resulting in a time series that showed no significant deviations from a constant brightness.

The intra-pixel sensitivity is also expected to contaminate the photometry in channel 2. However, we did not notice such a strong effect as seen in Channel 1. We concluded that the central star was localized on a part of the array which has a flat photometric response (pixel reference: 147.20,198.25). This part of the detector might be of particular interest for the warm *Spitzer* mission.

3.3. Transit light curve model with limb darkening (LD) corrections

We parameterized the transit light curve with 4 variables: the planet-star radius ratio R_p/R_* , the orbital distance to stellar radius ratio a/R_* , the impact parameter b , and the time of mid-transit T_c . We used the IDL transit routine OCCULTNL developed by Mandel & Agol (2002) for the transit light curve model.

For each channel, we calculated a theoretical limb-darkening model (Kurucz 1979) with $T_{\text{eff}} = 5000\text{K}$, $\log g = 4.5$, $[\text{Fe}/\text{H}]$ solar, and fit this model⁴ to derive the 4 non-linear limb-darkening coefficient defined by Claret (2000) and presented in Table 1. We found that accounting for the effects of limb-darkening decreased the resulting best-fit transit depth by 0.5σ at $8.0 \mu\text{m}$ to 1σ at $3.6 \mu\text{m}$. We tested the robustness of our result for several limb-darkening corrections. We derived planet-to-star radius ratios using linear and quadratic limb darkening coefficients. In these cases the resulting best-fit transit depth decreased by 0.4σ for channel 1 and 2 and by 0.8σ for channel 3 and 4 compared to a 4th degree polynomial limb-darkening corrections. Finally, we modified the values of the non-linear limb-darkening coefficients (Claret 2000) presented in Table 1 by 10% and found that the planet-to-star radius ratios changed by less than 0.5σ .

3.4. The fitting procedure

We performed a least-squares fit to our unbinned data over the whole parameter space (R_p/R_* , a/R_* , b , T_c , A_i , K_i). In order to find the best-fit observables to the data, we used the MPFIT package⁵, which performs a Levenberg-Marquardt least-squares fit. We combined the baseline function and the pixel-phase correction described above with the transit light curve function which takes limb darkening correction into account. We applied this method on the four channels independently to calculate the four observables.

3.5. Mean values and errors determination

We used a bootstrap method to determine the mean value, the statistical and systematical errors for the measured parameters. The possible presence of correlated noise in the light curve has to be considered (Pont et al. 2006).

⁴ See <http://kurucz.harvard.edu/grids/>

⁵ <http://cow.physics.wisc.edu/~craigm/idl/idl.html>

The bootstrap technique we used take into account both the red and white-noise. To estimate the systematic errors due to intrapixel sensitivity and baseline corrections, we randomly padded the beginning of the transit light curve from different phase before -0.03. Few thousand transit light curves with different baseline duration are produced that way. Additionally, we randomly varied each photometric measurement, within their estimated error bars, following a normal distribution in order to derive the statistical errors on the derived parameters. Totally, 4000 synthetic transit light curves were produced. We then fitted (Sect. 3.4) these transit light curves to derive a new set of parameters and to extract their means and their corresponding 1σ statistical and systematic errors.

As an additional test for the errors, we measured the errors using the Prayer Bead method (Moutou et al. 2004, Gillon et al. 2007). In this case, the residuals of the initial fit are shifted systematically and sequentially by one exposure, and then added to the eclipse model before fitting. The purpose of this procedure is to take into account the actual covariant noise level of the light curve. Using this method, we found negligible red-noise after corrections and obtained errorbars equivalent to the systematical and statistical errors derived with the bootstrap method presented above.

We examined the residuals from the best fit of each synthetic transit light curve and for each channel independently. We measured a RMS residual between 2.5 and 3.3×10^{-3} on normalized flux for all exposures, depending on the channel (See case of Channel 4 bottom panel Fig. 2). The RMS residuals are 20% larger than the expected photon-noise, and stays constant over the duration of the observation. We find that the scatter of residuals in binned exposures decreases with bin size as $N^{-1/2}$ for bins of up to 150 points for all the channels, as expected for photon-noise (See channel 1, bottom curve in Fig. 3).

4. RESULTS AND DISCUSSION

The results of the independent fits are given in Table 2. The most interesting parameters are the 4 planet-to-star radius ratios which are discussed in this section.

4.1. Comparisons with previous results

The main difference between our analysis of channels 1 and 3 and the previous studies (Ehrenreich et al. 2007, Beaulieu et al. 2008) resides in the pixel-phase decorrelation and baseline functions adopted.

In channel 1, the flux measured is strongly correlated with the position of the star on the detector array. We tested the influence of the pixel-phase decorrelation function on channel 1 by comparing a correction function with one parameter, as used in the previous studies (Ehrenreich et al. 2007; Beaulieu et al. 2008), to a 2nd degree function with 5 parameters as described in Sect. 3.2. For each corrected photometric time-series, the red noise was estimated as described in Gillon et al. (2006), by comparing the rms of the unbinned and binned residuals. In the case of channel 1, the fit is largely improved by fitting 5 parameters compared to only one parameter for the X and Y star position and only negligible systematics effects remain in the residuals (Fig. 3). Contrary to the two previous analysis, removing photo-

metric points which have an extreme pixel-phase value does not change our result, since they are well corrected by the present decorrelation methods. We thus kept all the photometric measurements.

The baselines are known to be inherently linear for channel 1 and 2 and logarithmic for channel 3 and 4 (Knutson et al. 2008). However, we tested three different baselines functions: polynomial of one, two and three degrees, an exponential with a polynomial, and logarithmic with a linear function as describe in Sect. 3.1. We tested the robustness of each of these different baselines using the same test as described in Ehrenreich et al. (2007), i.e. by dropping the first exposures from the beginning of the observations (exposure with a phase smaller than -0.03). We found that for channels 3 and 4, the best fits are obtained when using a logarithmic baseline (see lower panel in Fig. 2). In the case of a linear, polynomial or exponential baseline, the fitted parameters show large variations with the number of data point removed (Fig. 2, upper panel). The radius dramatically changes according to the number of points removed when using a linear or a third degree polynomial baseline functions indicating that systematics errors remain in the corrected data. In the case of a logarithmic baseline, the radius extracted does not depend on the number of removed points. The logarithmic function is the only one which allows the observable parameters to oscillate around the same value independently of removed exposures. Only small systematics still remain and they are included in the final error bar. Consequently, our estimates of the error bars on the measured parameters in channel 3 and 4 are conservative; they are larger by about 30% than the error bars due to the photon noise.

The present study shows that Ehrenreich et al. (2007) and Beaulieu et al. (2008) did not apply a sufficient pixel-phase decorrelation for channel 1. Consequently, systematics remained in these two previous studies (Fig. 3). Furthermore, none of these studies did use a logarithmic baseline for channel 3. This explains why Ehrenreich et al. (2007) obtained larger systematics error bars in this channel 3 when exploring this issue. Our analysis also shows that by using linear baselines, the result of Beaulieu et al. (2008) at $5.8 \mu\text{m}$ is affected by large systematics which are not included in their error bars estimations. Having understood the reasons of the discrepancies, the results in the present paper can be considered with most confidence.

The planet-to-star radius ratio at $8 \mu\text{m}$ that we derive (Fig. 4 and Table 2) is in agreement with a previous measurement obtained with the same instrument and same channel, but in subarray mode (Knutson et al. 2007a). The error bars we obtain are slightly larger, since they also includes systematic errors from the baseline (Fig. 2).

4.2. Discussion

We derived the fitted parameters and their error bars in a consistent way. From our fits, we evaluated at each wavelength the radius ratio R_p/R_* , the impact parameter b , the system scale a/R_* and the central time of the transit (Table 2).

The measured central time of the transit can be compared to the expected transit time from known ephemeris. Several observations of transits of HD 189733b have been published recently with improved

ephemeris (Bakos et al. 2006b; Winn et al. 2007a; Knutson et al. 2007; Pont et al. 2007; Knutson et al. 2009). We find that the central times that we obtained are in agreement within the error bars for each set of simultaneous observation, between channels 1 and 3 for the first epoch and channels 2 and 4 for the second one.

Although data from different channels have been fitted independently, our measurements of the impact parameter and of the system scale both show the same behavior as a function of the channel: they are consistent between channels observed simultaneously, but disagree between channels observed at the two different epochs. This strongly suggests that unrecognized systematics remains between the observations obtained at two epochs; these systematics could be of instrumental or more likely of astrophysical origin (e.g, star spots). We therefore consider that comparison of radius ratios should preferentially be made between measurements taken at the same epochs.

The impact parameter and the system scale values can also be compared with the most accurate measurements (Pont et al. 2007; $b = 0.671 \pm 0.008$ and $a/R_* = 8.92 \pm 0.009$), where the degeneracy between primary radius and orbital inclination could be lifted. Our results from our primary observations at $3.6 \mu\text{m}$ and $5.8 \mu\text{m}$ are in agreement with previous analysis of the same data set (Ehrenreich et al. 2007; Beaulieu et al. 2008), but are inconsistent at 3σ level with the Pont et al. (2007) values. This suggests that the measurements in these two channels may be affected by, for instance, stellar spots. The measurements of the impact parameter and the system scale in channels 2 and 4 data at $4.5 \mu\text{m}$ and $8 \mu\text{m}$ are in agreement with the measurements by Pont et al. (2007). This reinforces the confidence in our determination of the physical parameters for channels 2 and 4.

The planet-to-star radius ratio measured at $3.6 \mu\text{m}$ is larger than the value extrapolated from simultaneous measurements at $5.8 \mu\text{m}$ assuming that only water molecules contribute to the absorption in this channel. Therefore, other species must be present in the atmosphere of the planet and absorb at this wavelength. The possible presence of methane (CH_4) could also contribute to the opacity at $3.6 \mu\text{m}$. Interestingly, the planetary radius measured at this wavelength is in agreement with the extrapolation of the measurements obtained with HST/ACS in the visible (Pont et al. 2007, 2008) and assuming Rayleigh scattering as needed to interpret the large variations of the planet radius between 0.55 and $1.05 \mu\text{m}$ (Lecavelier des Etangs et al. 2008b).

Comparing the planet-to-star radius ratio obtained simultaneously in channels 2 and 4, we find a difference $(\Delta R_p/R_*)_{4.5-8 \mu\text{m}} = 0.00128 \pm 0.00056$. This corresponds to a 2.3σ signature of an excess absorption at $4.5 \mu\text{m}$ relative to $8 \mu\text{m}$. The radius at $4.5 \mu\text{m}$ is also 4σ above the expected value if only water molecules were contributing to the absorption in this channel (see Sect. 4.3). At this wavelength, another absorbent is needed. The new observations at $4.5 \mu\text{m}$ are not affected by the systematics one faces in at $3.6 \mu\text{m}$, mainly the pixel phase effect, since the central star was localized on a part of the array which has a flat photometric response. Hence data reduction and analysis of data taken in channel 2 at $4.5 \mu\text{m}$ are straight forward compared to data in the 3 other channels. As a consequence, the

parameter extraction in this channel is the most robust of the 4 channels; conclusions drawn from this channel can be considered with more confidence.

4.3. Possible CO signature and large C/O ratio scenario

From Fig. 4 and Table 2, a possible excess of absorption could be present in channel 2 around $4.5 \mu\text{m}$ by comparison with channel 4. At this wavelength, all main atmospheric constituents (H_2 , H_2O , CH_4) have no strong spectral features, except CO (Sharp & Burrows 2007; Fig 3). We therefore conclude that CO could be a candidate for identification of this possible absorption signature.

Following Eq. 2 of Lecavelier des Etangs et al. (2008a), if ΔR_p is the variation of the apparent planetary radius between channels 2 and 4, we have

$$\Delta R_p = H \ln \frac{\xi_2 \sigma_2}{\xi_4 \sigma_4},$$

where H is the atmospheric scale height, ξ and σ are the abundance and cross-section of the main absorbent in channels 2 and 4, respectively. For a temperature T , H is given by $H = kT/\mu g$, where μ is the mean mass of atmospheric particles taken to be 2.3 times the mass of the proton, and g the gravity. For HD 189733b, we have $H/R_* = 0.00045$ at 1500 K . With $\Delta R_p/R_* = 0.00128 \pm 0.00056$, we find

$$\log_{10} \frac{\xi_2 \sigma_2}{\xi_4 \sigma_4} = 1.245 \pm 0.540 \left(\frac{T}{1500 \text{ K}} \right)^{-1}.$$

The H_2O absorption cross-section is smaller in channel 2, $\sigma_{\text{H}_2\text{O}}(4.5 \mu\text{m}) = 2 \times 10^{-21} \text{ cm}^2/\text{molecule}$, than in channel 4, $\sigma_{\text{H}_2\text{O}}(8 \mu\text{m}) = 2 \times 10^{-20} \text{ cm}^2/\text{molecule}$ (Sharp & Burrows 2007). Therefore, assuming that H_2O is the main absorbent at $8 \mu\text{m}$, we find that the planet-to-star radius ratio at $4.5 \mu\text{m}$ should be $(R_p/R_*)_{4.5 \mu\text{m}} = 0.1534 \pm 0.0005$. This value is 4σ below our effective measurement. Therefore, species other than H_2O should be present. Because CO has a strong absorption signature at this wavelength, it is a possible candidate for explaining the larger planetary radius measured at $4.5 \mu\text{m}$.

CO has a similar cross section at $4.5 \mu\text{m}$ as water at $8 \mu\text{m}$: $\sigma_{\text{H}_2\text{O}}(8 \mu\text{m}) = \sigma_{\text{CO}}(4.5 \mu\text{m}) = 2 \times 10^{-20} \text{ cm}^2/\text{molecule}$, therefore, the two measurements in channels 2 and 4 lead to the conclusion that

$$\log_{10} \xi_{\text{CO}}/\xi_{\text{H}_2\text{O}} = 1.245 \pm 0.540 \left(\frac{T}{1500 \text{ K}} \right)^{-1}.$$

This corresponds to CO abundance of 5 to 60 times the H_2O abundance. Note that the lower limit of the CO/ H_2O ratio (~ 6) is about 3.5σ higher than the highest ratio at which CO absorption at $4.5 \mu\text{m}$ are overcome by H_2O absorption (CO/ $\text{H}_2\text{O} = 0.1$). In other words, at CO/ H_2O ratio above $= 0.1$, CO is the main absorbent and can be detected at $4.5 \mu\text{m}$; our measurements show an absorption 3.5σ above this level.

A C/O ratio above the solar value could enhance, at high temperature, the CO abundance with respect to the abundance of H_2O in the atmosphere of HD189733b (Tinetti et al. 2007). Indeed, carbon-rich planetary environments do exist: a C/O ratio much larger than solar has been measured with *FUSE* and *HST* in the planetary system of β Pictoris (Jolly et al. 1998; Lecavelier des Etangs et al. 2001; Roberge et al.

2006). Planets evolving in such environments could have a high C/O ratio in their atmospheres. The large CO/H₂O ratio would appear at odd with the detection of CH₄ claimed by Swain et al. (2008), though the presence of CO is more consistent with the temperature above 1000 K as estimated from primary and secondary transit observations. Furthermore, simulations show that vigorous dynamics caused by uneven heating of tidally locked planets can homogenize the CO and CH₄ concentrations (Cooper & Showman 2006). However, recent 3D models (Showman et al. 2008) shows that the planet could experience dramatic day/night temperature variations along the planetary limb. As a consequence, the detection of both CO and CH₄ molecules by primary transit observations could be compatible if they are located in different limb regions.

5. SUMMARY

We have performed and analyzed new *Spitzer*/IRAC primary eclipse observations of HD 189733b at 4.5 μ m and 8 μ m and reanalyzed observations at 3.6 μ m and 5.8 μ m in a consistent way. Our analysis is more robust against systematics than the previous ones (Ehrenreich et al. 2007, Beaulieu et al. 2008), especially regarding the pixel-phase effect and baseline correction. Systematic error corrections can now be applied in all channels.

As a consequence, contrary to what was claimed in a previous study, we do not find the excess absorption at 5.8 μ m compared to 3.6 μ m that was initially found by Beaulieu et al. (2008) and interpreted by water absorption by Tinetti et al. (2007). Therefore, other species such as methane must be present in the atmosphere of the planet and absorb at this wavelength. Noteworthy,

the measured radius at 3.6 μ m is compatible with the radius extrapolated assuming Rayleigh scattering absorption by small particles.

Interestingly in channel 2, the star is centered in a region of the array which has a flat photometric response. Therefore, the resulting measurements in this channel are robust.

Comparing the planet-to-star radius ratios obtained simultaneously at 4.5 and 8 μ m, we noticed a 2.3 σ excess absorption at 4.5 μ m. Furthermore, the radius ratio at 4.5 μ m stands 4 σ above the expected value if only water molecules were contributing to the absorption. If this signature is confirmed, it could be interpreted by absorption by CO molecules. In that case, we estimate a ratio of CO/H₂O abundances of 5 to 60, possibly indicating a high C/O ratio.

The Near Infrared Spectrograph (NIRSpec) aboard the future *James Webb Space Telescope* will enable medium-resolution spectra over a wavelength range from 1 to 5 μ m and thus allow for clear identification simultaneously and unambiguously of H₂O, CH₄, CO and CO₂.

We thank the referee who greatly contributed to improve the paper, as well as H. Knutson and Ph. Nutzman for helpful discussion on data reduction and analysis. D.K.S. is supported by CNES. This work is based on observations made with the *Spitzer Space Telescope*, which is operated by the Jet Propulsion Laboratory, California Institute of Technology under a contract with NASA. D.E. acknowledges financial support from the French *Agence Nationale pour la Recherche* through ANR project NT05-4.44463.

REFERENCES

- Agol, E., Cowan, N. B., Bushong, J., Knutson, H., Charbonneau, D., et al. 2008, arXiv:0807.2434
- Bakos, G. Á., Knutson, H., Pont, F., Moutou, C., Charbonneau, D., et al. 2006b, *ApJ*, 650, 1160
- Bakos, G. Á., Pál, A., Latham, D. W., Noyes, R. W., & Stefanik, R. P. 2006a, *ApJ*, 641, L57
- Ballester, G. E., Sing, D. K., & Herbert, F. 2007, *Nature*, 445, 511
- Barman, T. S., Hauschildt, P. H., & Allard, F. 2005, *ApJ*, 632, 1132
- Beaulieu, J. P., Carey, S., Ribas, I., & Tinetti, G. 2008, *ApJ*, 677, 1343
- Bouchy, F., et al. 2005, *A&A*, 444, L15
- Brown, T. M. 2001, *ApJ*, 553, 1006
- Brown, T. M., Libbrecht, K. G., & Charbonneau, D. 2002, *PASP*, 114, 826
- Burrows, A., Hubbard, W. B., Lunine, J. I., & Liebert, J. 2001, *Reviews of Modern Physics*, 73, 719
- Charbonneau, D., Allen, L. E., Megeath, S. T., et al. 2005, *ApJ*, 626, 523
- Charbonneau, D., Brown, T. M., Noyes, R. W., & Gilliland, R. L. 2002, *ApJ*, 568, 377
- Claret, A. 2000, *A&A*, 363, 1081
- Cooper, C. S., & Showman, A. P. 2006, *ApJ*, 649, 1048
- Deming, D., Harrington, J., Laughlin, G., et al. 2007, *ApJ*, 667, L199
- Deming, D., Harrington, J., Seager, S., & Richardson, L. J. 2006, *ApJ*, 644, 560
- Deming, D., Brown, T. M., Charbonneau, D., Harrington, J., & Richardson, L. J. 2005, *ApJ*, 622, 1149
- Deming, D., Seager, S., Richardson, L. J., & Harrington, J. 2005, *Nature*, 434, 740
- Deming, D., Brown, T. M., Charbonneau, D., Harrington, J., & Richardson, L. J. 2005, *ApJ*, 622, 1149
- Désert, J.-M., Vidal-Madjar, A., Lecavelier Des Etangs, A., Sing, D., Ehrenreich, D., et al. 2008, *A&A*, 492, 585
- Ehrenreich, D., Lecavelier des Etangs, A., Hébrard, G., et al. 2008, *A&A*, 483, 933
- Ehrenreich, D., Hébrard, G., Lecavelier des Etangs, A., et al. 2007, *ApJ*, 668, L179
- Ehrenreich, D., Tinetti, G., Lecavelier des Etangs, A., Vidal-Madjar, A., & Selsis, F. 2006, *A&A*, 448, 379
- Hébrard, G., & Lecavelier des Etangs, A. 2006, *A&A*, 445, 341
- Fazio, G. G., et al. 2004, *ApJS*, 154, 10
- Fortney, J. J., & Marley, M. S. 2007, *ApJ*, 666, L45
- Gillon, M., Pont, F., Demory, B.-O., et al. 2007, *A&A*, 472, L13
- Gillon, M., Demory, B.-O., Barman, T., et al. 2007, *A&A*, 471, L51
- Gillon, M., Pont, F., Moutou, C., Bouchy, F., Courbin, F., et al. 2006, *A&A*, 459, 249
- Grillmair, C. J., Burrows, A., Charbonneau, D., Armus, L., Stauffer, J., et al. 2008, *Nature*, 456, 767
- Harrington, J., Luszcz, S., Seager, S., Deming, D., & Richardson, L. J. 2007, *Nature*, 447, 691
- Horne, K. 1986, *PASP*, 98, 609
- Hébrard, G., & Lecavelier des Etangs, A. 2006, *A&A*, 445, 341
- Hubbard, W. B., Fortney, J. J., Lunine, J. I., et al. 2001, *ApJ*, 560, 413
- Jolly, A., McPhate, J. B., Lecavelier des Etangs, A., et al. 1998, *A&A*, 329, 1028
- Kuchner, M. J., & Seager, S. 2005, arXiv:astro-ph/0504214
- Knutson, H. A., Charbonneau, D., Cowan, N. B., Fortney, J. J., Showman, A. P., et al. 2009, *ApJ*, 690, 822
- Knutson, H. A., Charbonneau, D., Noyes, R. W., Brown, T. M., & Gilliland, R. L. 2007a, *ApJ*, 655, 564
- Knutson, H. A., et al. 2007b, *Nature*, 447, 183
- Kurucz, R. L. 1979, *ApJS*, 40, 1
- Kurucz, R. 2006, *Stellar Model and Associated Spectra* (<http://kurucz.harvard.edu/grids.html>)

- Lecavelier des Etangs, A., Vidal-Madjar, A., Roberge, A., et al. 2001, *Nature*, 412, 706
- Lecavelier des Etangs, A., Pont, F., Vidal-Madjar, A., & Sing, D. 2008a, *A&A*, 481, L83
- Lecavelier des Etangs, A., Vidal-Madjar, A., Désert, J.-M., & Sing, D. 2008b, *A&A*, 485, 865
- Liang, M.-C., Parkinson, C. D., Lee, A. Y.-T., Yung, Y. L., & Seager, S. 2003, *ApJ*, 596, L247
- Liang, M.-C., Seager, S., Parkinson, C. D., Lee, A. Y.-T., & Yung, Y. L. 2004, *ApJ*, 605, L61
- Mandel, K., & Agol, E. 2002, *ApJ*, 580, L171
- Moutou, C., Pont, F., Bouchy, F., & Mayor, M. 2004, *A&A*, 424, L31
- Morales-Calderón, et al. 2006, *ApJ*, 653, 1454
- Naylor, T. 1998, *MNRAS*, 296, 339
- Pont, F., Zucker, S., & Queloz, D. 2006, *MNRAS*, 373, 231
- Pont, F., Gilliland, R. L., Moutou, C., Charbonneau, D., Bouchy, F., et al. 2007, *A&A*, 476, 1347
- Pont, F., Knutson, H., Gilliland, R. L., Moutou, C., & Charbonneau, D. 2008, *MNRAS*, 385, 109
- Reach, W. T., et al. 2006, *IRAC Data Handbook v3.0*
- Redfield, S., Endl, M., Cochran, W. D., & Koesterke, L. 2008, *ApJ*, 673, L87
- Richardson, L. J., Harrington, J., Seager, S., & Deming, D. 2006, *ApJ*, 649, 1043
- Roberge, A., Feldman, P. D., Weinberger, A. J., Deleuil, M., & Bouret, J.-C. 2006, *Nature*, 441, 724
- Seager, S., & Sasselov, D. D. 2000, *ApJ*, 537, 916
- Sing, D. K., Vidal-Madjar, A., Désert, J.-M., Lecavelier des Etangs, A., & Ballester, G. 2008a, *ApJ*, 686, 658
- Sing, D. K., Vidal-Madjar, A., Lecavelier des Etangs, A., et al. 2008b, *ApJ*, 686, 667
- Sharp, C. M., & Burrows, A. 2007, *ApJS*, 168, 140
- Showman, A. P., Fortney, J. J., Lian, Y., Marley, M. S., Freedman, R. S., et al. 2008, *arXiv:0809.2089*
- Swain, M. R., Vasisht, G., & Tinetti, G. 2008, *Nature*, 452, 329
- Swain, M. R., Vasisht, G., Tinetti, G., Bouwman, J., Chen, P., et al. 2009, *ApJ*, 690, L114
- Tinetti, G., Liang, M.-C., Vidal-Madjar, A., Ehrenreich, D., Lecavelier des Etangs, A., Yung, Y. L. 2007a, *ApJ*, 654, L99
- Tinetti, G., et al. 2007b, *Nature*, 448, 169
- Vidal-Madjar, A., Lecavelier des Etangs, A., Désert, J.-M., et al. 2008, *ApJ*, 676, L57
- Vidal-Madjar, A., et al. 2004, *ApJ*, 604, L69
- Vidal-Madjar, A., Lecavelier des Etangs, A., Désert, J.-M., Ballester, G. E., Ferlet, R., Hébrard, G., & Mayor, M. 2003, *Nature*, 422, 143
- Werner, M. W. et al., 2004, *ApJS*, 154, 1
- Winn, J. N., et al. 2007, *AJ*, 133, 1828

TABLE 1. LIMB DARKENING COEFFICIENTS

| IRAC Channel | Wavelength | C1 | C2 | C3 | C4 |
|--------------|-------------------|--------|---------|--------|---------|
| 1 | 3.6 μm | 0.6023 | -0.5110 | 0.4655 | -0.1752 |
| 2 | 4.5 μm | 0.6886 | -0.8869 | 0.8504 | -0.3077 |
| 3 | 5.8 μm | 0.7138 | -1.0720 | 1.0515 | -0.3825 |
| 4 | 8 μm | 0.5497 | -0.8042 | 0.7698 | -0.2719 |

TABLE 2. FITTING PARAMETERS OF THE TRANSIT CURVES

| Parameter | 3.6 μm (Ch 1) | 4.5 μm (Ch 2) | 5.8 μm (Ch 3) | 8 μm (Ch 4) |
|--------------------|--------------------------|--------------------------|--------------------------|------------------------|
| R_p/R_* | 0.15449 | 0.15565 | 0.15466 | 0.15437 |
| $\sigma(R_p/R_*)$ | ± 0.00031 | ± 0.00033 | ± 0.00054 | ± 0.00045 |
| b | 0.6327 | 0.6562 | 0.6279 | 0.6651 |
| $\sigma(b)$ | ± 0.0099 | ± 0.0076 | ± 0.0111 | ± 0.0060 |
| a/R_* | 9.136 | 8.940 | 9.257 | 8.890 |
| $\sigma(a/R_*)$ | ± 0.091 | ± 0.077 | ± 0.107 | ± 0.069 |
| $T_0(HJD)$ | 2454039.82881 | 2454428.08128 | 2454039.82895 | 2454428.08151 |
| $\sigma(T_0)(HJD)$ | ± 0.00009 | ± 0.00011 | ± 0.00013 | ± 0.00009 |

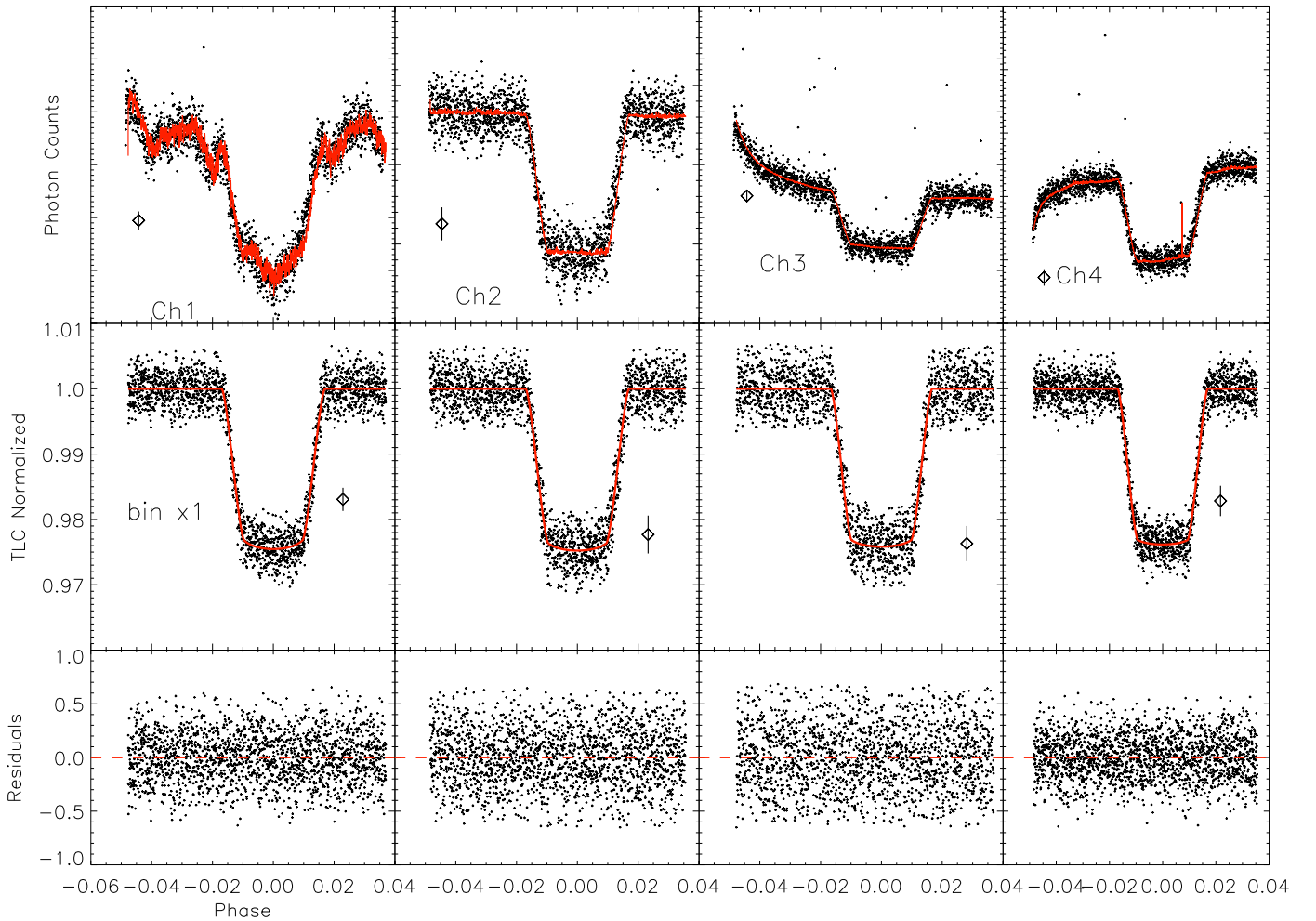


FIG. 1.— Transit light curves, fits and residuals for each channel. Data are not rebinned. Typical 1σ error bars on individual measurements are represented. The raw weighted light curves (top panel) have to be corrected for large fluctuations correlated to the ‘pixel phase’ and to the ramp baseline. The corrected light curve is plotted in the middle panel without the rejected points (rejection at more than 3σ). Overplotted is the fit with limb darkening taken into account. The bottom plot show the residuals from the best fits.

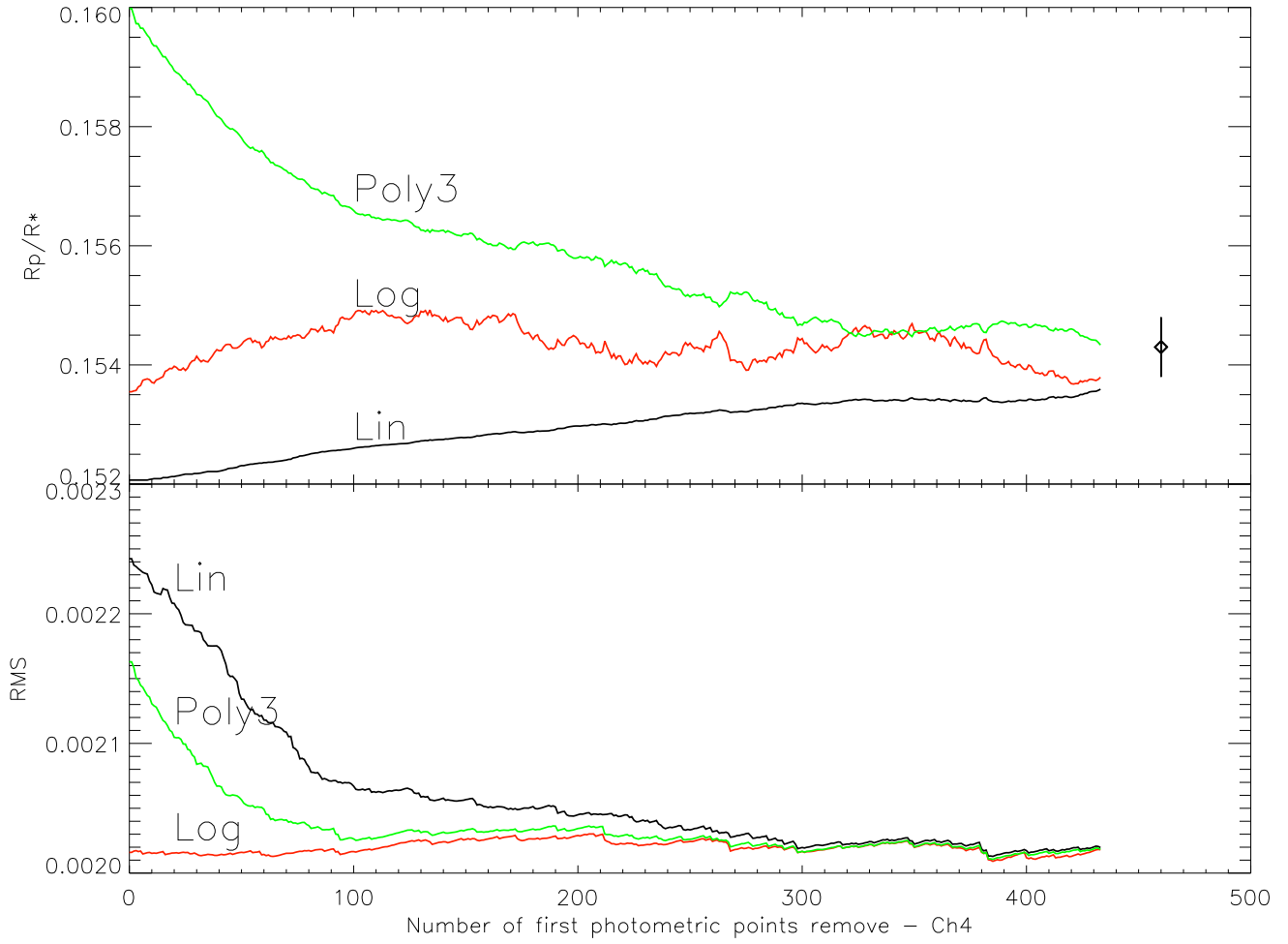


FIG. 2.— Channel 4. Top panel: R_p/R_* ratios extracted when using linear, polynomial of a 3rd degree, and logarithmic baselines as function of the number of first photometric points removed from which the transit light curve is fitted. In the abscisse, 0 point removed correspond to the full transit light curve (TLC). The left over TLC when padded at a phase of -0.03 correspond to the removal of ~ 430 measured points. The diamond point on the right hand side with its error bar, indicates the mean value with its error bar obtained by bootstrap when using a logarithmic baseline (Sect. 3.5). Bottom panel: Root-mean-square (RMS) resulting from the fit using the three different baselines describe above as function of first exposures removed. The fit is always better when using the logarithmic function. This is particularly true at the beginning of the time series, where the ramp effect is the strongest (See Sect. 3.1).

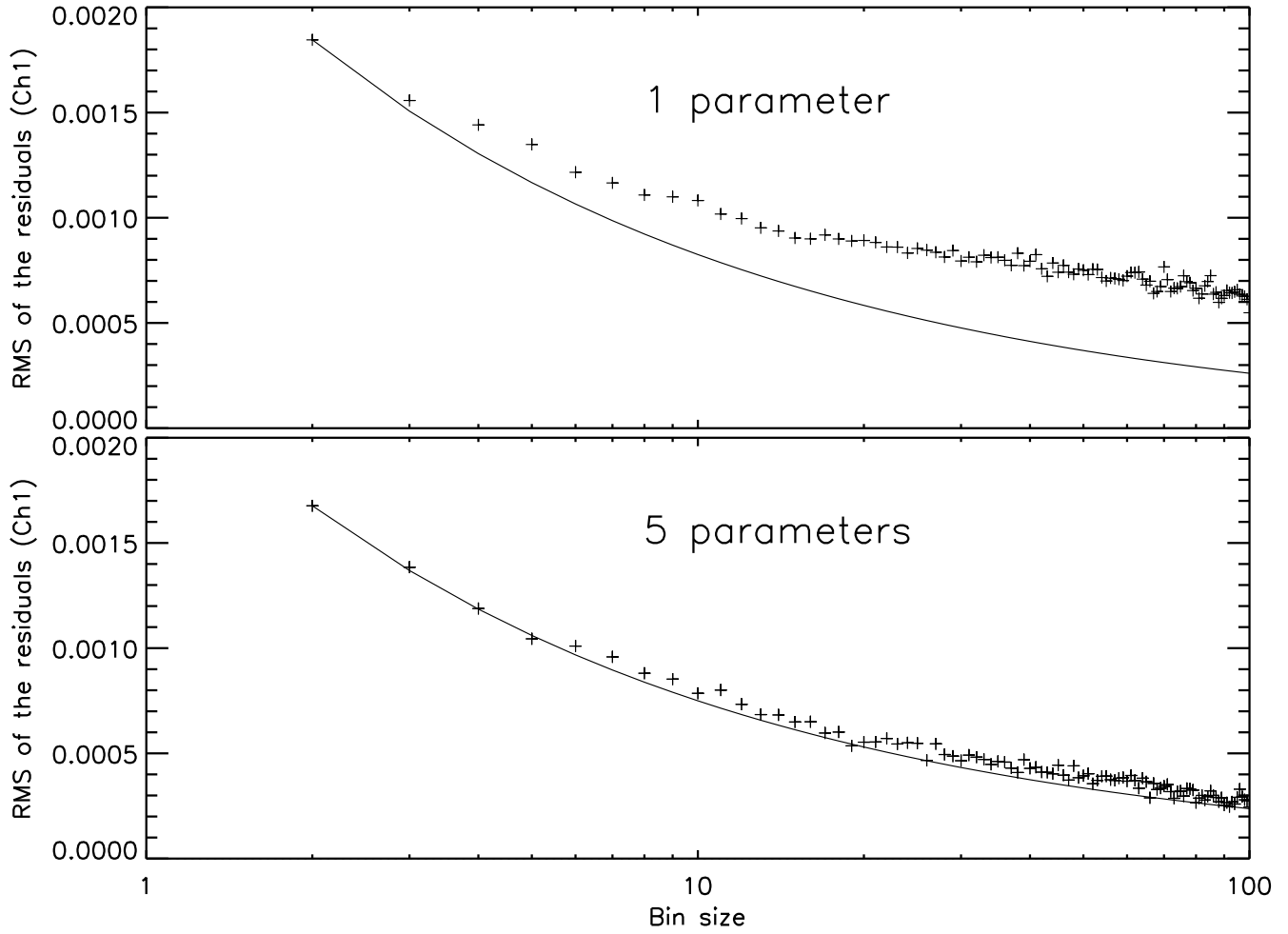


FIG. 3.— Root-mean-square (RMS) of binned residuals versus bin size for channel 1 for two different pixel-phase effect decorrelation. The solid line is proportional to $N^{-1/2}$. Top panel: RMS resulting from the fit with 1 parameter used to fit the corrective coefficient in the X and Y direction axis. Bottom panel: RMS resulting from the a quadratic fit with 5 parameters. Negligible systematics appear in the residuals when using 5 parameters to characterize the pixel-phase effect.

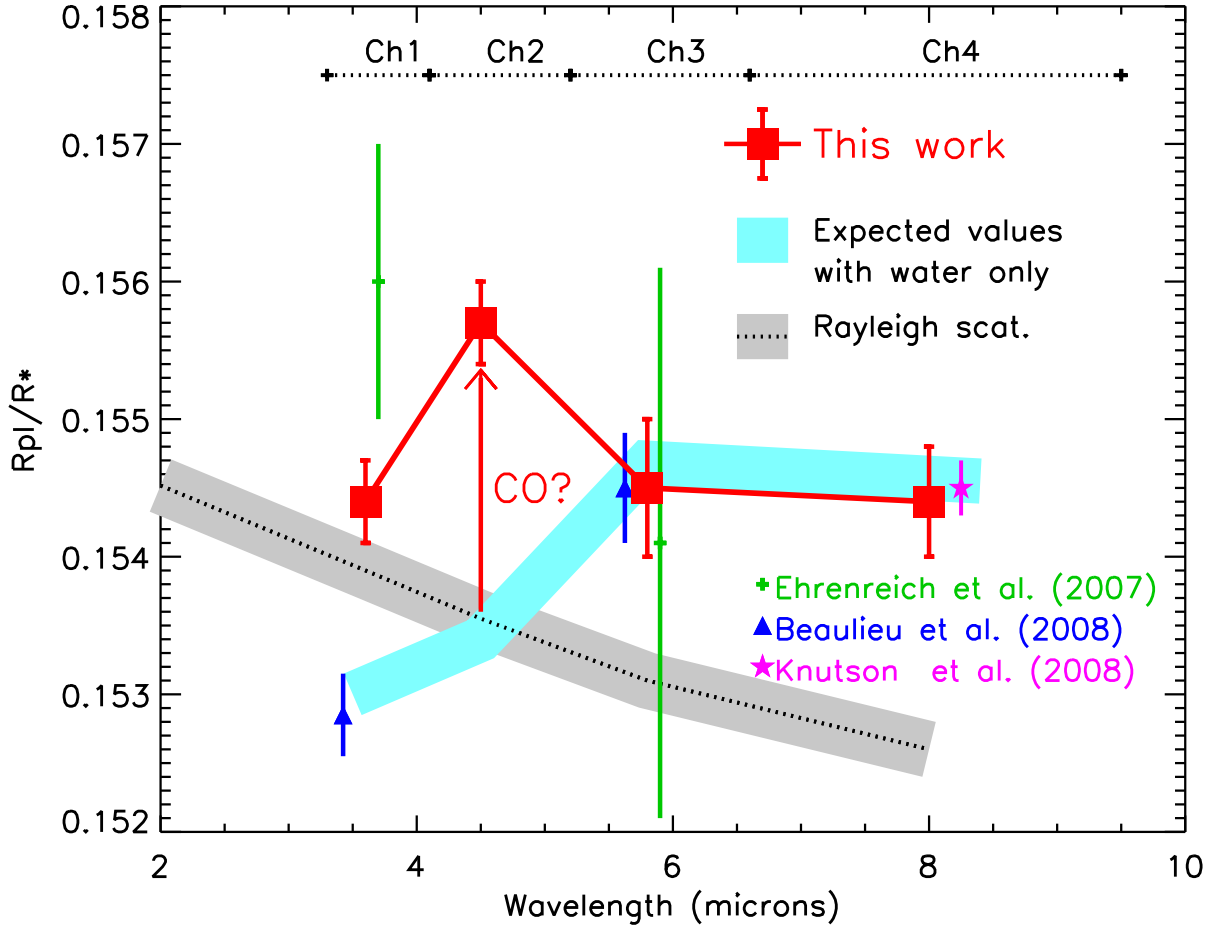


FIG. 4.— Measured values of R_p/R_* ratios in the four *Spitzer*/IRAC channels for HD 189733b. Results in channel 1 at 3.6 μm and in channel 3 at 5.8 μm are from the same data sets but from different analysis (Ehrenreich et al. 2007, Beaulieu et al. 2008, and this work). Our analysis presented in this paper is more robust against systematics than the previous ones. New observations in channel 2 at 4.5 μm and in channel 4 at 8.0 μm are also presented here. Results from our present analysis are plotted with red squares. Previous estimates from the same dataset at 3.6 μm and at 5.8 μm are plotted with green dots (Ehrenreich et al. 2007) and with blue triangles (Beaulieu et al. 2008). An independent measurement from Knutson et al. (2007a) at 8 μm in Channel 4 is plotted with a purple star. The R_p/R_* ratio obtained at 4.5 μm is larger (4σ) than expected with either water absorption only (light blue line) or with Rayleigh scattering by small particles (grey dotted line; Pont et al. 2008; Lecavelier des Etangs et al. 2008a). Therefore, other species must be present in the atmosphere of the planet absorbing at this wavelength. This supplementary absorption could be due to the presence of CO molecules in the planetary atmosphere.